ACS Catalysis

Research Article

pubs.acs.org/acscatalysis

Carbon Corrosion in Proton-Exchange Membrane Fuel Cells: Effect of the Carbon Structure, the Degradation Protocol, and the Gas Atmosphere

Luis Castanheira,[†,‡] Wanderson O. Silva,[§] Fabio H.B. Lima,[§] Alexandre Crisci,[Δ,⊥] Laetitia Dubau,*[,†,‡] and Frédéric Maillard*[,†,‡]

[†]Univ. Grenoble Alpes, LEPMI, F-38000 Grenoble, France

[‡]CNRS, LEPMI, F-38000 Grenoble, France

[§]Instituto de Química de São Carlos, Universidade de São Paulo, CEP 13560-970, CP 780 São Carlos, SP, Brazil

[Δ]Univ. Grenoble Alpes, SIMAP, F-38000 Grenoble, France

[⊥]CNRS, SIMAP, F-38000 Grenoble, France

Supporting Information

ABSTRACT: The impact of the carbon structure, the aging protocol, and the gas atmosphere on the degradation of Pt/C electrocatalysts were studied by electrochemical and spectroscopic methods. Pt nanocrystallites loaded onto high-surface area carbon (HSAC), Vulcan XC72, or reinforced-graphite (RG) with identical Pt weight fraction (40 wt %) were submitted to two accelerated stress test (AST) protocols from the Fuel Cell Commercialization Conference of Japan (FCCJ) mimicking load-cycling or start-up/shutdown events in a proton-exchange membrane fuel cell (PEMFC). The load-cycling protocol essentially caused dissolution/redeposition and migration/aggregation/coalescence of the Pt nanocrystallites but led to similar electrochemically active surface area (ECSA) losses for the three Pt/C electrocatalysts. This suggests that the nature of the carbon support plays a minor role in the potential range $0.60 < E < 1.0$ V versus RHE. In contrast, the carbon support was strongly corroded under the start-up/shutdown protocol ($1.0 < E < 1.5$ V versus RHE), resulting in pronounced detachment of the Pt nanocrystallites and massive ECSA losses. Raman spectroscopy and differential electrochemical mass spectrometry were used to shed light on the underlying corrosion mechanisms of structurally ordered and disordered carbon supports in this potential region. Although for Pt/HSAC the start-up/shutdown protocol resulted into preferential oxidation of the more disorganized domains of the carbon support, new structural defects were generated at quasi-graphitic crystallites for Pt/RG. Pt/Vulcan represented an intermediate case. Finally, we show that oxygen affects the surface chemistry of the carbon supports but negligibly influences the ECSA losses for both aging protocols.

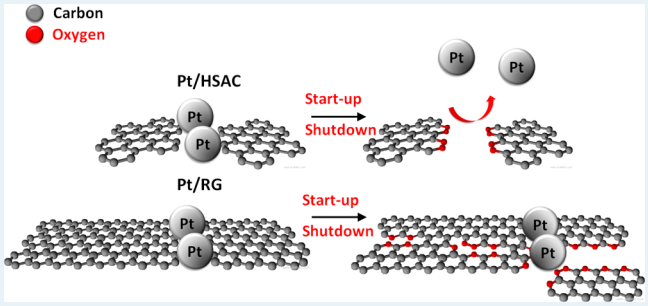

KEYWORDS: *proton-exchange membrane fuel cells (PEMFCs), carbon corrosion, catalyst support corrosion, accelerated stress testing, durability of PEMFC materials, degradation mechanisms*

In the search for renewable energy sources, different possibilities (solar power plants, wind turbines, geothermal, and ocean energy) are currently being implemented. The largest drawback for renewable energy sources is their intermittency, which implies the need of flexible electrochemical storage and conversion systems to accommodate the energy demand. Hydrogen (H_2), with a mass energy density of 140 MJ kg^{-1},[1] is the most relevant contender to store renewable electrical energy produced in excess in the H−H bond. In case the energy demand exceeds the production, this chemical energy may then be converted back into electrical energy thanks to a proton-exchange membrane fuel cell (PEMFC).[2] However, PEMFCs still suffer from the insufficient durability of their constitutive materials: the carbon supported Pt or Pt-M nanocrystallites (Pt/C or Pt-M/C, M being an early or late transition metal) used as electrocatalysts, the proton-exchange membrane (PEM), the ionomer, and the gas-diffusion layers.[3−5] The physicochemical and electrochemical analyses performed on aged membrane electrode assemblies[4−17] or model PEMFC electrodes aged in accelerated stress tests protocols (ASTs)[14,18−22] have unveiled several degradation mechanisms for the Pt-based nanocrystallites: (i) dissolution/redeposition via electrochemical Ostwald ripening,[23,24] (ii) chemical reduction of the Pt^{z+} ions produced by the electrochemical Ostwald ripening into electrically disconnected Pt crystallites in the proton-exchange membrane or in the

Received: December 9, 2014
Revised: February 16, 2015
Published: February 23, 2015

DOI: 10.1021/cs501973j
ACS Catal. 2015, 5, 2184−2194

ionomer of the catalytic layer,[4,23,24] (iii) migration/aggregation/coalescence of the Pt-based nanocrystallites,[4,25−28] and (iv) the electrochemical oxidation of the carbon support (carbon oxidation reaction − COR).[4,29−32]

The COR is of prime importance for the long-term stability of the electrocatalytic materials. This reaction is thermodynamically possible at a PEMFC cathode ($E^0_{CO_2/C}$ = 0.207 V versus the normal hydrogen electrode (NHE) at T = 298 K), but its rate becomes significant only at electrode potentials higher than 1.0−1.1 V versus NHE.[23,29,31−35] These conditions are encountered during localized fuel starvation[13,36] or PEMFC start-up/shutdown events[13,37,38] and result in massive corrosion of the carbon support and collapse of the electrode structure.[4−6,14,21,22,28] In the potential range 0.6 < E < 1.0 V versus the reversible hydrogen electrode (RHE), it has been shown that the COR is catalyzed by the presence of Pt nanoparticles, most likely via the back-spillover of oxygen-containing surface groups (CO_{surf}) to the metal surface followed by their oxidation into CO_2.[29,31,33] The gas atmosphere also plays a decisive role: Dubau et al.[14] have shown that the electrochemically active surface area (ECSA) losses are enhanced during potential cycling between 0.05 < E < 0.50 V versus RHE in oxygen atmosphere with respect to the same degradation protocol conducted in an inert atmosphere. This was rationalized by considering the production of hydroperoxyl and hydroxyl species during the oxygen reduction reaction (ORR) in this potential region. The structural parameters of the carbon support (in-plane mean carbon crystallite size (L_a), crystallite size in the direction perpendicular to the quasi-graphitic layers (L_c), and interlayer spacing (d_{002})), the carbon specific surface area, the micropore and mesopore volume, and the surface chemistry of the carbon supports also strongly influence the COR kinetics.[39] Stonehart et. al[40,41] conducted one of the first studies bridging carbon structure and COR kinetics in phosphoric acid at T = 473 K. The authors reported that heat-treated carbons (graphitized carbons) possess smaller interplanar distances (d_{002}) than the pristine carbon support and are less prone to electrochemical corrosion. Cherstiouk et al.[42] studied the robustness of different carbon supports, amorphous (carbon blacks) and graphitic carbons (nanofilaments), in sulfuric acid at T = 353 K and E = 1.2 V versus RHE. The authors monitored large COR currents for small and disordered graphitic crystallites with high interplanar distances. Recently, Artyushkova et al.[43] pointed out that these structural parameters are not enough to predict the resistance to corrosion of high surface area carbon supports. The authors suggested an interesting relationship between structural and chemical parameters, hydrophilicity/hydrophobicity, and electrochemical activity for the ORR and resistance to the COR. The carbon samples with high graphitic content, small BET surface area, low amount of carbon surface oxides, and large amount of elongated and large-sized pores were found to be more electrochemically active for the ORR and less reactive toward the COR.[43] However, a systematic study investigating the interplay between carbon nanostructure, initial and final dispersion of the metal nanocrystallites, and ECSA losses under AST conditions is still lacking, and these aspects are the focus of the present work.

Here, Pt nanocrystallites loaded onto high-surface area carbon (HSAC), Vulcan XC72, or reinforced-graphite (RG) with identical Pt weight fraction (40 wt %) were submitted to two accelerated stress test (AST) protocols from the Fuel Cell Commercialization Conference of Japan (FCCJ) under neutral (argon) or oxidizing atmosphere (oxygen) at T = 330 K. Electrochemical characterizations allowed quantifying the ECSA losses and determining the variation of the charge associated with the quinone/hydroquinone (Q/HQ) redox peak. The structural changes in the Pt/C electrocatalysts were monitored by transmission electron microscopy (TEM) and Raman spectroscopy.

EXPERIMENTAL SECTION

Electrocatalysts. Pt nanoparticles supported onto (i) a high-surface-area carbon (TEC10E40E), (ii) Vulcan XC72 (TEC10V40E), or (iii) reinforced graphite (TEC10EA40E) were supplied by Tanaka Kikinzoku (TKK). The electrocatalysts had a Pt weight fraction (wt %) of 40% and were used as received.

Porosity and Surface Area Measurements. The textural characteristics of carbons were obtained from the nitrogen adsorption measurements performed at T = 77 K with an automatic volumetric device ASAP 2020 (Micromeritics). The samples were pretreated from T = 363 to 573 K (1 K min^{-1}) and kept during 180 min at T = 573 K. The analysis of the adsorption isotherms provided the BET specific surface area S_{BET} (in the range P/P_0 = 0.05−0.2), the total pore volume V_Σ (at P/P_0 = 0.98), and the micropore volume V_μ (here P_0 is the saturation pressure). The values of the mean pore diameter D_{BET} were calculated on the basis of the BET model as D_{BET} = 4 V/S.

X-ray Diffraction Measurements. The synthesized and reference electrocatalysts were analyzed using a PANalytical X'Pert Pro MPD vertical goniometer/diffractometer equipped with a diffracted-beam monochromator using Cu Kα radiation (λ = 0.15418 nm) operating at 45 kV and 40 mA. The 2θ angle extended from 10 to 125° and varied using a step size of 0.033° accumulating data for 525s. The interlayer spacing (d_{002}) and the crystallite size in the direction perpendicular to graphene layers (L_c) were calculated from the two-dimensional (002) lattice reflection of graphite at 2$\theta \sim$ 24°.

Transmission Electron Microscopy (TEM) Imaging. The fresh and the aged Pt/C nanoparticles were examined with a Jeol 2010 TEM operated at 200 kV with a point to point resolution of 0.19 nm. After the electrochemical experiments, the catalytic layer was scraped from the glassy carbon, dispersed in MQ-water and deposited onto a gold grid (300 mesh, Lacey Carbon; Agar Sc. U.K.) for TEM observations.

Raman Spectroscopy. Raman spectroscopy was used to examine the structure of the fresh and aged carbon supports. The Raman spectra were recorded ex situ using either a Renishaw RM1000 or a Renishaw In-Via spectrometer. They were obtained by excitation with the radiation from an argon LASER (514 nm) operated at approximately 5 mW. The detector was a Peltier-cooled charge coupled device camera and the spectral resolution was 1 cm^{-1}. The measurements were performed with a 50× ULWD objective and a 100 μm confocal aperture for both the sample illumination and collection of the scattered photons. For the sake of comparison, the Raman spectra of the Pt/C electrocatalysts were normalized to the intensity of the peak at ca. 1585 cm^{-1}, which corresponds to the band of the graphitic lattice. The curve fitting of the Raman spectra was performed with the software LabSpec, and five bands were considered (Table 1). Averages from at least five spectra are reported.

DOI: 10.1021/cs501973j
ACS Catal. 2015, 5, 2184−2194

Table 1. Vibration Modes Observed on High Surface Area Carbon Supports with Raman Spectroscopy

band	Raman shift	vibration mode
G	ca. 1585 cm^{-1}	ideal graphitic lattice
D1	ca. 1350 cm^{-1}	disordered graphitic lattice−graphene layer edge
D2	ca. 1610 cm^{-1}	disordered graphitic lattice−surface graphene layer
D3	ca. 1495 cm^{-1}	amorphous carbon
D4	ca. 1190 cm^{-1}	polyenes, ionic impurities

The mean in-plane crystallite size of the carbon particles was obtained using the Knight and White formula:[44]

$$L_a(\mathrm{nm}) = 4.4 \times (I_{D1}/I_G)^{-1} \quad (1)$$

Solutions. All the glassware used in this study was first cleaned by immersion in a H_2SO_4/H_2O_2 mixture and thoroughly rinsed with MQ-grade water before use. The solutions were prepared from ultrapure water (MQ grade, 18.2 MΩ cm, 1−3 ppm TOC) and H_2SO_4 (Suprapur, Merck). As shown by a study from Takahashi et al.,[45] similar durability trends are observed in perchloric acid and sulfuric acid, and therefore, our results hold practical interest for both electrolytes. However, due to hindered specific adsorption of O(H) groups,[46] and the formation of complexes between Pt^{z+} ions (z = 2, 4) and (bi)sulfate ions, ECSA losses are heightened in sulfuric acid. Moreover, it is very well-known that (bi)sulfate anions better mimic the degradation of the sulfonated end groups of Nafion used as a solid electrolyte in real PEMFC devices.[5,23] For these two reasons, a 0.1 M H_2SO_4 solution purged with argon (99.99%, Messer) was chosen as electrolyte.

Electrochemical Measurements in Conventional Glass Cells. The electrochemical characterization of the Pt/C electrocatalysts and the AST were conducted in two separated four-electrode electrochemical glass cells, a characterization and a degradation cell, both thermostated at T = 330 K. A homemade rotating disk electrode (RDE) tip was used as working electrode. The counter electrode was a glassy carbon plate, and the reference electrode—a mercury sulfate electrode (MSE) $Hg|Hg_2SO_4|K_2SO_4$ (saturated, aqueous)—connected to the cell via a Luggin capillary. This reference electrode was calibrated periodically by measuring its potential difference with a reversible hydrogen electrode (RHE), which was systematically 0.72 V. A Pt wire connected to the reference electrode was used to filter the high frequency electrical noise and to avoid disturbing the low frequency electrical measurements. Additional details on the dual-reference system used in this work can be found in ref 47.

Preparation of the Catalytic Layers. A suspension with a concentration of 0.735 $g_{Pt/C}$ L^{-1} composed of 5 wt % Nafion solution (Aldrich), MQ-grade water, and Pt/C electrocatalyst (40 wt % Pt/HSAC, Pt/Vulcan or Pt/RG) was ultrasonically treated for 15 min to obtain a well-dispersed ink. Before each degradation test, the ink was ultrasonically treated for 6 min. A calibrated drop of 20 μL of this ink was deposited onto a homemade RDE made of glassy carbon (Sigradur, 0.196 cm^2) and Teflon resulting in a Pt loading of 30 μg_{Pt} cm^{-2}, and dried for 5 min at T = 383 K in air to ensure evaporation of the water and the Nafion solvents, resulting in a so-called "porous" RDE. Before the electrochemical measurements, the working electrode was immersed in the electrochemical cell at controlled electrode potential E = 0.40 V versus RHE.

Electrochemical Characterization. Ten cyclic voltammograms were first recorded at v = 0.02 V s^{-1} between E = 0.05 and 1.23 V versus RHE followed by a cyclic voltammogram at v = 0.1 V s^{-1}, and a CO_{ad} stripping voltammogram in the same potential range was then performed to obtain the characteristic voltammetric response of the Pt/C electrocatalysts. After the electrochemical characterization, the electrode was withdrawn at controlled electrode potential E = 0.40 V versus RHE and transferred to the degradation cell with the electrode surface protected by a drop of electrolyte to avoid any contamination.

Accelerated Stress Tests. To investigate the effect of the potential range and the gas atmosphere on the degradation of the Pt/C electrocatalysts, ASTs derived from the FCCJ organization were performed.[18] The tests consisted of two protocols: (i) a load-cycling protocol, where the electrode potential was modulated with a square wave and stepped between 0.6 and 1.0 V versus RHE with a holding time of 3 s at each voltage and (ii) a start-up/shutdown protocol, where the electrode potential was modulated with a square wave and stepped between 1.0 and 1.5 V versus RHE with a holding time of 3 s at each voltage (different from the conventional FCCJ protocol, where the electrode potential is linearly swept between 1.0 and 1.5 V versus RHE with a rate of v = 0.5 V s^{-1}). A total of 5000 potential cycles were performed in the "degradation cell" under argon or oxygen atmosphere, and intermediate characterizations were performed after 100, 250, 500, 1000, 2500, and 5000 cycles to monitor the ECSA losses and the variation of the intensity of the Q/HQ redox peak. The RDE was not rotated during the AST. To limit the negative impact of intermediate characterizations,[48] only five cyclic voltammograms at v = 0.1 V s^{-1} and two cyclic voltammograms at v = 0.02 V s^{-1} were performed. The variation of ECSA over time was calculated by integrating the coulometry required to desorb under-potentially deposited hydrogen ($Q_{H,des}$), assuming a charge density of 210 μC cm^{-2} for a saturated layer of adsorbed H. To calculate the charge of the Q/HQ redox peak, a straight line between 0.40 V < E < 0.77 V versus RHE was used as a background.

Differential Electrochemical Mass Spectrometry (DEMS) Experiments. In DEMS experiments, a suspension with a concentration of 1 $g_{Pt/C}$ L^{-1} of Pt/C, composed of 5 wt % Nafion solution (Aldrich), MQ-grade water, and 40 wt % Pt/C was ultrasonically treated for 15 min to obtain a well-dispersed ink. Thin-film working electrodes were then prepared by depositing 180 μL of this suspension onto a gold layer (1.13 cm^2 area, 50 nm thickness), obtained by Au sputtering onto a Gore-Tex PTFE membrane (pore size 0.02 μm), resulting in ca. 60 μg_{Pt} cm^{-2}. Water was then evaporated at T = 383 K, and the electrodes were immersed in the electrochemical cell. Online DEMS measurements were performed with a Pfeiffer Vacuum QMA 200 quadrupole mass spectrometer using a setup consisting of two differentially pumping chambers. This technique allowed online detection of carbon dioxide (CO_2) produced during the COR. In the experiments, the current versus potential curves were recorded simultaneously with the mass intensity versus potential curves, for selected values of the mass/charge (m/z) ratio. The CO_2 produced during the COR was monitored at m/z = 44 (CO_2^+). The m/z = 2 (H_2^+) and m/z = 22 (doubly ionized CO_2 − CO_2^{2+}) signals were also recorded.

RESULTS AND DISCUSSION

Figure 1a,b display the normalized Raman and the X-ray diffraction spectra of the different carbon supports, respectively. The vibrational band appearing at ca. 1585 cm^{-1}, namely, the G

DOI: 10.1021/cs501973j
ACS Catal. 2015, 5, 2184−2194

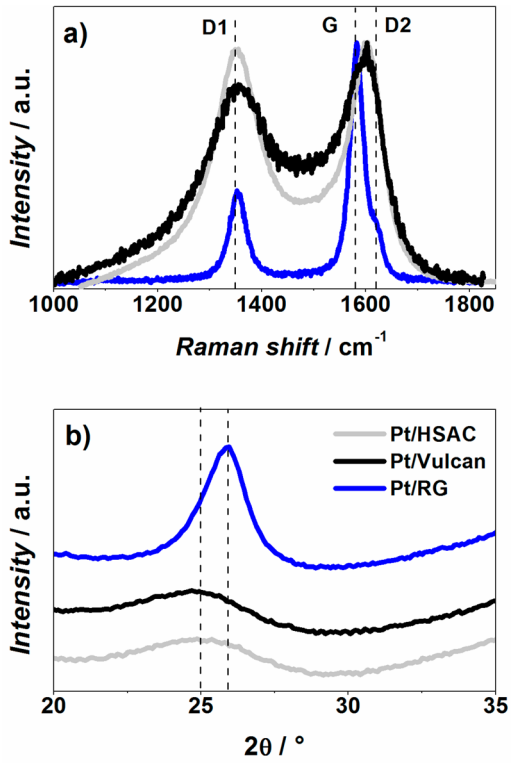

Figure 1. (a) Normalized Raman spectra and (b) zoom on the (002) reflection line of the X-ray diffraction spectra of Pt/HSAC, Pt/Vulcan and Pt/RG electrocatalysts. The Raman spectra are normalized to the intensity of the G band; therefore any change in the proportion of ordered/disordered carbon domains graphically results into modified D1 and G band frequency/shape.

band, is assigned to the quasi-graphitic crystallites, and the D1 band at ca. 1350 cm^{-1} is assigned to the edge-defects on these crystallites.[35,44,49−51] Note that the Raman spectra are normalized to the intensity of the G band; therefore, any change in the proportion of ordered/disordered carbon domains graphically results into modified D1 and G band frequency/shape.

Pronounced differences are noticed between the spectra of the carbon blacks and the RG support. The superior intensity and the broader D1 band for the HSAC and the Vulcan supports reflect their lower level of structural ordering relative to RG.[49,50] The position and the shape of the G band depend on the analyzed carbon material: on RG, it is sharp and close to the value reported for graphite single crystal ($\bar{\upsilon}$∼ 1575 cm^{-1});[49] however, for HSAC and Vulcan, this band is broader and blue-shifted (i.e., shifted to higher wavenumber values). This is due to the increasing contribution of the D2 band at ca. $\bar{\upsilon}$∼ 1615 cm^{-1}, which is assigned to structural defects in the surface of the graphite crystallites.[50,51] The average in-plane mean carbon crystallite size (L_a) of the different supports was estimated using the Knight and White formula:[44] the carbon blacks supports (HSAC and Vulcan) featured L_a value in the order of 0.8 and 1.0 nm, respectively. The in-plane dimension of carbon was 9.4 nm for the reinforced graphite support (Table 2).

In the XRD spectra (Figure 1b), the (002) reflection line of carbon was found to be broader for the carbon blacks relative to the RG support due to strain and the smaller crystallite size in the direction perpendicular to the graphene layers (L_c). The estimated average interlayer spacing (d_{002}) of RG was higher than that reported for pure graphite (0.335 nm) but significantly less than that of Vulcan XC72 and HSAC (see Table 2). Note that d_{002} values of carbon blacks represent an average interlayer spacing value due to the turbostratic stacking of the support. The crystallite size in the direction perpendicular to the graphene layers, determined from the half-width of the (002) reflection line, was identical for Pt/HSAC and Pt/Vulcan and larger for Pt/RG in agreement with its more ordered structure. Despite similar L_a, L_c, and d_{002} values, the Vulcan and HSAC supports featured different BET specific surface areas (S_{BET}, see Table 2): this reflects different weight proportion of amorphous and disordered carbon domains present between and within the quasi-graphitic crystallites.

Because the S_{BET} values of Pt/HSAC and Pt/Vulcan were found smaller than those of the raw carbon supports (i.e., before Pt deposition, see Table 2), we assumed that the Pt nanocrystallites preferentially sit in the structurally disordered domains of the carbon black support or at the edges of the quasi-graphitic layers in agreement with the early hypothesis of Bett et al.[52] The S_{BET} values for the Pt/C electrocatalysts decreased in the order Pt/HSAC ≫ Pt/Vulcan XC72 ∼ Pt/RG, thus translating differences in the micropore, and mesopore content. This parameter is of prime interest as it determines to what extent Pt nanocrystallites are free to move on the carbon support before colliding and agglomerating with a neighboring Pt crystallite.

Table 2. Textural and Substructural Properties of the Carbon Supports Investigated in This Study[a]

		40 wt % Pt/HSAC TKK	40 wt % Pt/Vulcan TKK	40 wt % Pt/RG TKK
textural characteristics	BET surface area of the carbon support provided by the supplier ($S_{BET,\ supplier}$)/$m^2\ g^{-1}_{carbon}$	800	250	-
	measured BET surface area of the Pt/C nanoparticles ($S_{BET,\ measured}$)/ $m^2\ g^{-1}_{carbon}$	462	136	110
	total pore volume (V_Σ)/ $cm^3\ g^{-1}_{carbon}$	0.497	0.188	0.307
	micropore volume (V_μ)/ $cm^3\ g^{-1}_{carbon}$	0.034	0.019	0.004
	mean pore diameter (D_{BET})/nm	4.3	5.5	11.1
substructural parameters	L_a/nm	0.8	0.9	9.4
	L_c/nm	2.3	2.4	4.2
	d_{002}/ nm	0.357	0.360	0.346
chemical parameters	O1s/C1s ratio (from X-ray photoelectron spectroscopy)	0.11	0.24	0.08

[a] L_a− the average in-plane mean carbon crystallite size; L_c − crystallite size in the direction perpendicular to graphene layers; d_{002} − interlayer spacing.

DOI: 10.1021/cs501973j
ACS Catal. 2015, 5, 2184−2194

Representative TEM images of the fresh Pt/HSAC, Pt/Vulcan and Pt/RG are displayed in Figure 2. The HSAC and

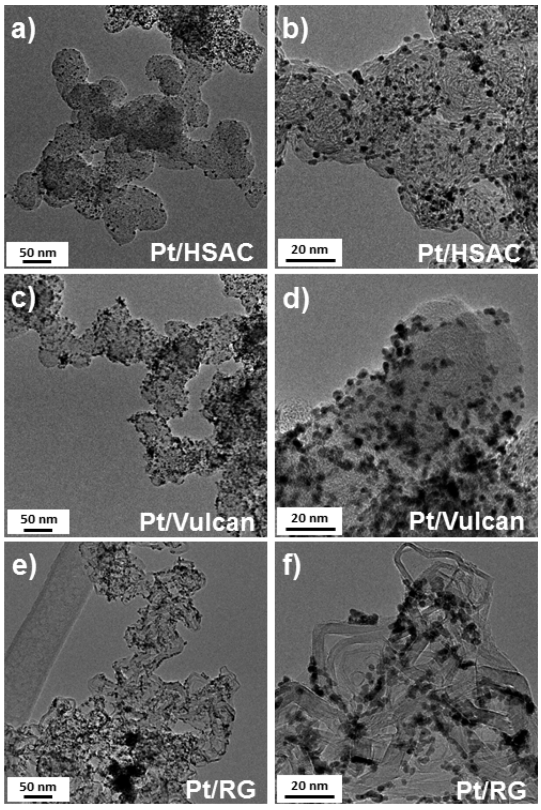

Figure 2. TEM images of the different Pt/C electrocatalysts: (a, b) Pt/HSAC, (c, d) Pt/Vulcan, (e, f) Pt/RG.

the Vulcan supports (Figure 2b,d) feature round-shaped primary carbon particles with size between 10 and 100 nm. These primary carbon particles are composed of quasi-graphitic crystallites, which are stacked roughly parallel to one another at the particle surface and arranged in a more disorderly fashion toward the particle center. These observations agree with the (002) lattice fringes monitored in XRD spectra, and the carbon black concentric microstructure model first proposed by Heckman et al.[53] In contrast, the larger lateral dimensions of the carbon nanocrystallites (see Table 2) and the increasing contrast of the (002) lattice fringes in TEM for Pt/RG (Figure 2f) reflect its higher degree of graphitization.[39,54,55] As depicted in Figure 2, graphitization resulted in a decrease in the average dimensions of the carbon primary particles and the agglomerates, as well as the collapse of the micropores located between the quasi-graphitic crystallites. These changes in texture influence the dispersion and the degree of agglomeration of the Pt/C nanocrystallites: it is clear from Figure 2 that high micropore content and S_{BET} value result in highly dispersed and evenly distributed Pt nanocrystallites onto the carbon support, in agreement with literature data.[56−60] At identical Pt weight percentage (40 wt %), the Pt specific surface area (S_{Pt}) equals 55 ± 14 m^2 g^{-1}Pt for Pt/HSAC, 41 ± 5 m^2 g^{-1}Pt for Pt/Vulcan and 40 ± 11 m^2 g^{-1}Pt for Pt/RG. As we will show, the best electrocatalysts in the native state are not necessarily the most stable.

The robustness of the Pt/HSAC, the Pt/Vulcan, and the Pt/RG electrocatalysts was evaluated by performing ASTs in argon or oxygen saturated 0.1 M H_2SO_4 at T = 330 K. The ASTs consisted of 5000 square potential cycles between 0.6 and 1.0 V versus RHE with a holding time of 3 s at each potential (load-cycling protocol) or 5000 square potential cycles between 1.0 and 1.5 V versus RHE with a holding time of 3 s at each potential (start-up/shutdown protocol). The first protocol mimics the potential range experienced by a PEMFC cathode during normal operation. The second protocol mimics excursions to high potential 1.0 < E ≤ 1.5 V versus RHE experienced by the cathode electrocatalyst during start/stop or fuel starvation events.[13,37,38,61,62] Indeed, because air is used to flush hydrogen from the anode during a PEMFC stop, high cathode potentials are produced by the simultaneous presence of hydrogen/air and air/air fronts in the anode compartment.[37] Note that high cathode potentials may also be faced when water droplets temporarily block the channels of the bipolar plates ("fuel starvation" conditions).

Figure 3 displays intermediate cyclic voltammograms (CVs) recorded during ASTs under neutral atmosphere. The CVs feature the underpotential deposition of protons (H_{upd}), and adsorption of oxygenated species regions between 0.05 < E < 0.40 V versus RHE and for E > 0.75 V versus RHE, respectively. The broad oxidation/reduction peak in the potential range 0.5 < E < 0.8 V versus RHE is ascribed to electron transfer on/from quinone/hydroquinone (Q/HQ) groups.[39]

The ECSA losses against the number of potential cycles are monitored in Figure 4. Three general observations can be made: first, the ECSA losses depend on the electrochemical potential range experienced by the Pt/C electrocatalysts; second, the structure of the carbon support determines the extent of Pt/C degradation during the start-up/shutdown protocol; and third, oxygen has a negligible effect on the ECSA losses both under load-cycling and start-up/shutdown protocols. It was no surprise to note that larger ECSA losses were monitored during the start-up/shutdown relative to the load-cycling protocol.[31,32,34,37,63] A striking point, however, is that similar losses were obtained for all types of carbon support during the load-cycling protocol (note the small differences after 2500 potential cycles in Figure 4a,c). Coupled to minor variations of the Q/HQ electrical charge and of the double layer capacitance (these parameters depend strongly on the specific surface area and on the surface chemistry of the supports, see refs 39,64), this result suggests that carbon corrosion is not the predominant degradation mechanism in these operating conditions but that other factors such as electrochemical Ostwald ripening and crystallite migration/aggregation/coalescence determine the ECSA losses, in agreement with previous findings.[14,23,26,27,35,48,65]

The scenario is opposite during the start-up/shutdown protocol where the structure of the carbon support is key. The ECSA losses amount to 60/80% for the Pt/Vulcan and the Pt/HSAC electrocatalysts, respectively, and only to 25% for the Pt/RG. These results agree with former literature reports that graphitic carbon supports are more robust than disordered carbon supports at electrode potentials E > 1.0 V versus RHE.[42,55,66−68] Besides, in the case of the Pt/RG electrocatalyst, the homothetic variations of the H_{upd} and O adsorption/desorption features, coupled to the minor variations of the double layer capacitance of the electrode, strongly suggest that the Pt nanocrystallites simply detached from the carbon support during this protocol.

Another interesting observation was the fact that ECSA losses were nearly independent of the AST protocol for the Pt/

DOI: 10.1021/cs501973j
ACS Catal. 2015, 5, 2184−2194

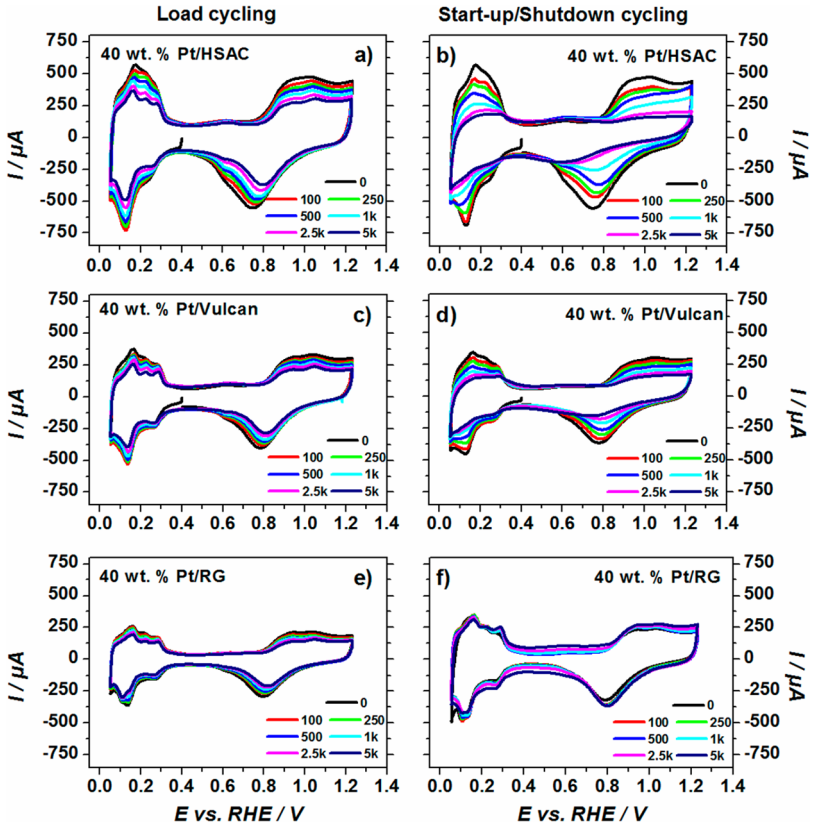

Figure 3. Intermediate characterization cyclic voltammograms measured on the Pt/C electrocatalysts during (a, c, e) load-cycling and (b, d, f) start-up/shutdown aging protocols. The numbers in the caption refer to the number of potential cycles during the AST. Electrolyte: 0.1 M H_2SO_4; v = 0.020 V s^{-1}; T = 330 K. The RDE was not rotated during the AST.

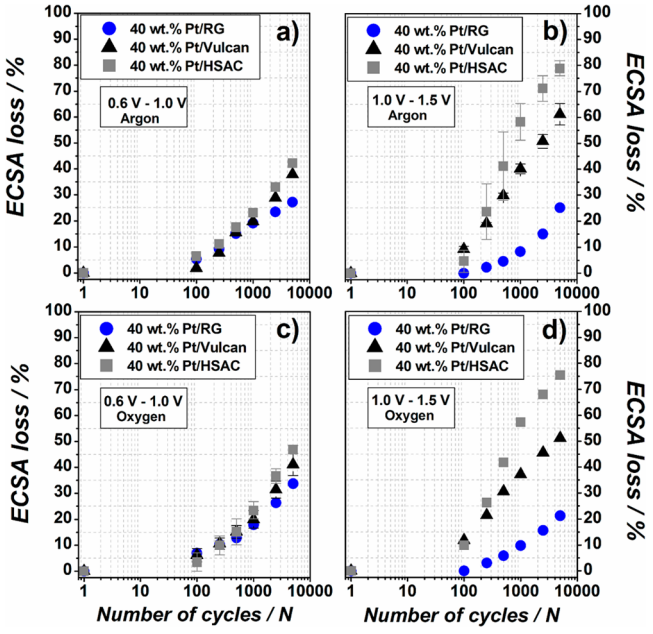

Figure 4. ECSA losses monitored for the 40 wt % Pt/HSAC, the 40 wt % Pt/Vulcan and the 40 wt % Pt/RG electrocatalysts during the FCCJ protocols under (a, b) argon or (c, d) oxygen atmosphere. Electrolyte: 0.1 M H_2SO_4; v = 0.100 V s^{-1}; T = 330 K. The RDE was not rotated during the AST. The error bars represent the standard deviations of ECSA losses.

RG electrocatalyst. As noticed previously, the Pt crystallites are highly agglomerated on this support (Figure 2). This intrinsic characteristic minimizes the proportion of ECSA, which can be lost by migration/agglomeration of the Pt nanocrystallites, but does not prevent the electrochemical Ostwald ripening to operate during load-cycling (see similar broadening of the particle size distribution for all Pt/C electrocatalysts in Figure S1). In contrast, the particle size distribution showed almost no broadening during the start-up/shutdown protocol, thus confirming our previous hypothesis that ECSA losses are governed by the electrochemical Ostwald ripening and the detachment of the Pt nanocrystallites in these experimental conditions.

Finally, it is interesting to note that similar ECSA losses were monitored in neutral (Figure 4a,b) and in oxidizing atmosphere (Figure 4c,d) for all AST protocols. This suggests that oxygen plays no decisive role on the ECSA losses during load-cycling and start-up/shutdown protocols in liquid electrolyte. It is extremely important to point out that different aging mechanisms and different extent of degradation were recently noticed in solid polymer and in liquid electrolyte.[65] However, considering that migration, aggregation and detachment of the metal nanocrystallites, and redeposition of Pt^{z+} ions are more pronounced in a solid polymer electrolyte, we believe that this conclusion is transferable to real PEMFC devices. Note however that oxygen influences the degradation of Pt/C electrocatalysts in the potential range 0.05 < E < 0.50 V versus RHE[14] due to the two-electron pathway of the ORR in this potential region, which generates radical species and damages carbon black supports.

To better understand the impact of the AST protocols, the variations of the electrical charge under the quinone-hydro-

DOI: 10.1021/cs501973j
ACS Catal. 2015, 5, 2184−2194

quinone (Q/HQ) redox peak were monitored over time. Figure 5 shows that the variations of the Q/HQ charge (i)

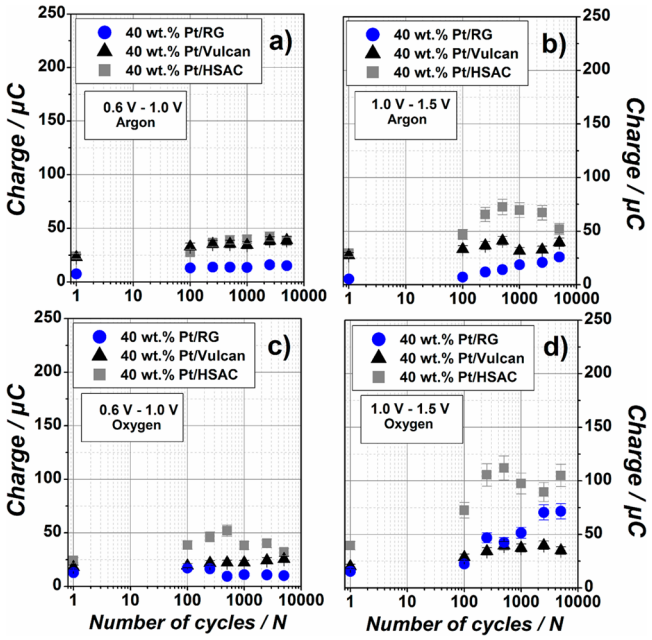

Figure 5. Variation of the electrical charge of the quinone-hydroquinone redox peak monitored for the 40 wt % Pt/HSAC, the 40 wt % Pt/Vulcan, and the 40 wt % Pt/RG electrocatalysts during the FCCJ protocols under (a, b) argon or (c, d) oxygen atmosphere. To calculate the charge of the Q/HQ redox peak, a straight-line between 0.40 V < E < 0.77 V versus RHE was used as a background. The error bar was estimated to be ±10%.

depend on the applied AST protocol, (ii) are not monotonic, and (iii) depend on the gas atmosphere. Under argon atmosphere, a slight increase of the Q/HQ electrical charge was noticed during the load-cycling protocol for the less organized supports, but no variation was visible on the RG support. During the start-up/shutdown protocol, a gradual increase of the Q/HQ charge was observed for the three carbon supports until a maximum was reached after which the electrical charge was decreasing. Interestingly, the number of potential cycles needed to reach this maximum is inversely proportional to the mean crystallite size of the carbon support (see Table 2) and to its BET surface area: a maximal value of the Q/HQ charge was observed after ca. 500 cycles for the HSAC and the Vulcan supports, and a continuous increase was observed on the RG support under argon atmosphere. Performing the ASTs under oxidizing atmosphere amplified the experimental trends for the less organized carbon supports; however, the variations of the Q/HQ electrical charge were not proportional to the final ECSA losses. This is an important conclusion because the H/HQ charge is sometimes the unique parameter used to quantify the extent of degradation of different carbon supports.

We then strived to gain fundamental insights into how the structure of the carbon supports was degraded in the different potential ranges and under the different gas atmospheres. To this end, the ratio between the intensities of the D1 and G bands (I_D/I_G) in Raman spectroscopy was used as a structural marker (Tuinstra and Koenig first evidenced that this ratio is linearly proportional to the inverse of the in-plane carbon mean crystallite size L_a[49]). Figure 6 displays normalized Raman spectra monitored on the Pt/C electrocatalysts before/after

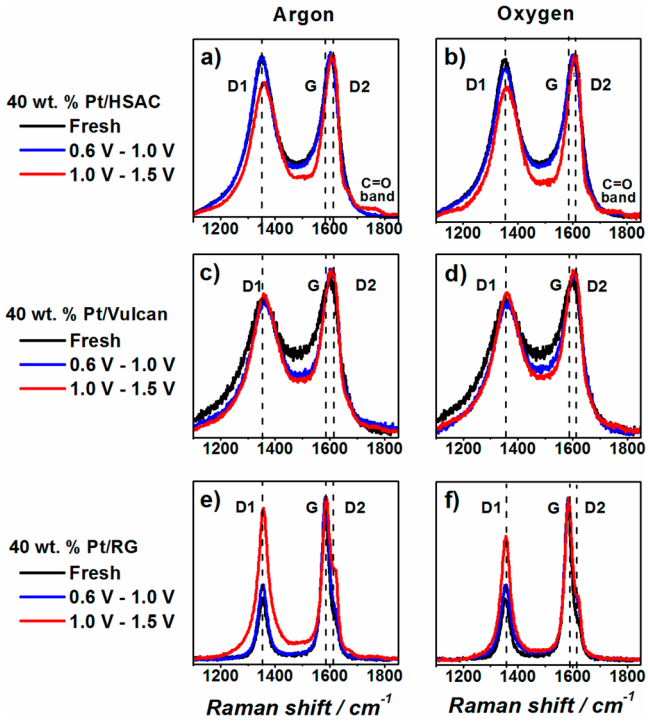

Figure 6. Normalized Raman spectra of the Pt/HSAC, Pt/Vulcan and Pt/RG electrocatalysts before/after the ASTs protocols under (a, c, e) argon or (b, d, f) oxygen atmosphere. Averages from at least five spectra are reported.

aging (note that averages from five spectra are reported). Although almost no change was evidenced in the Raman spectra of the Pt/HSAC electrocatalyst subjected to the load-cycling protocol, a pronounced decrease in the intensity of the D1 band was observed during the start-up/shutdown protocol. This result indicates that the disorganized domains of the HSAC support are preferentially oxidized during the COR, in agreement with our previous findings.[35,69] A shoulder is visible at $\overline{\upsilon}$~ 1760 cm^{-1} after the start-up/shutdown aging protocol under argon atmosphere. This band is ascribed to the C═O stretching vibration of carbonyl groups in carboxylic acids, or lactone,[51,70,71] and suggests that the HSAC surface becomes more oxidized in these aging conditions. Different trends were observed for the Pt/RG electrocatalyst. A slight increase of the D1 band intensity was observed after the load-cycling protocol, suggesting that edge-type defects were formed in the quasi-graphitic crystallites. The formation of the edge-defects was intensified during the start-up/shutdown protocol and, at the same time, was accompanied by the formation of surface-defects (increase of the D2 band intensity at $\overline{\upsilon}$~ 1610 cm^{-1}). Interestingly, this behavior was maintained under oxygen atmosphere; however, the lower intensities of the D1 and the D2 Raman bands indicate that structural defects were fastly corroded in these AST conditions. The Pt/Vulcan electrocatalyst is an intermediate case between Pt/HSAC and Pt/RG. The preferential corrosion of the most disordered regions during load-cycling or start-up/shutdown protocols appears compensated by the generation of new edge defects. In consequence, the shape and the intensity of the D1 (edge-defects) and G bands remained similar, and the G band slightly blueshifted, as a result of the increasing contribution of the D2 band intensity (formation of surface-defects).

DOI: 10.1021/cs501973j
ACS Catal. 2015, 5, 2184−2194

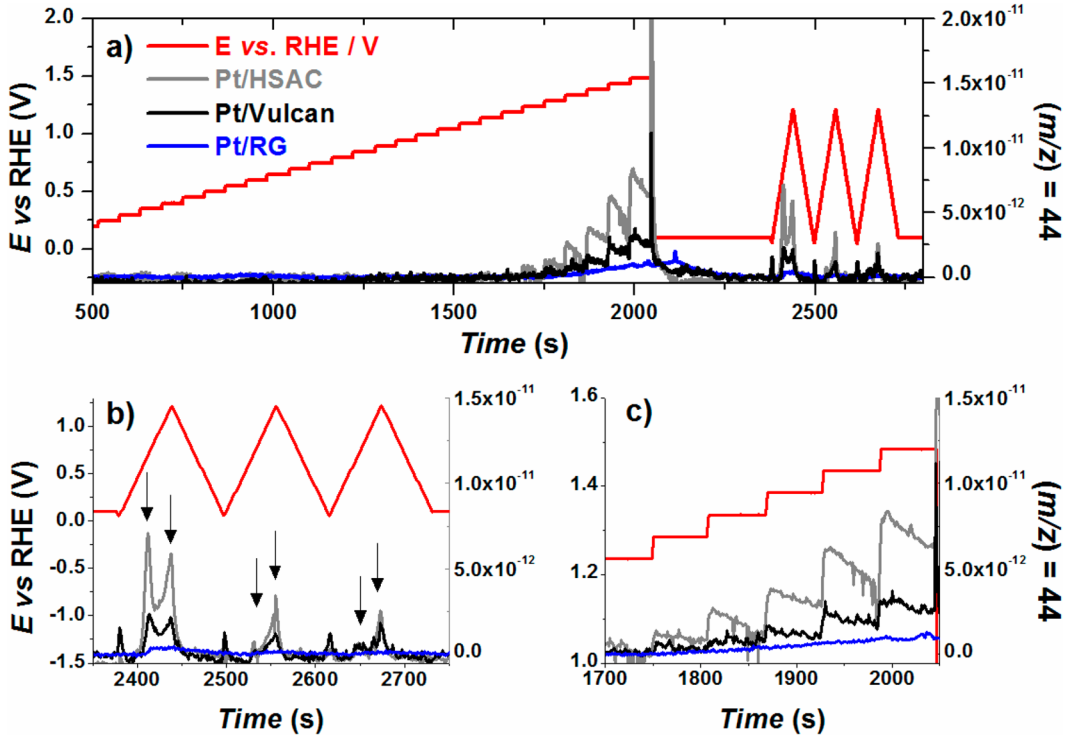

Figure 7. Mass intensity/potential-curves during (a, c) a potential ramp from 0.4 to 1.5 V versus RHE (0.05 V steps −30 s each) and (b) three subsequent cyclic voltammograms at a potential sweep rate v = 0.020 V s^{-1}. Ar-saturated solution, T = 330 K. m/z = 44.

To further understand the origin of the structure-dependent ECSA losses during the start-up/shutdown protocol, the quantities of CO_2, which were released during a potential ramp from 0.4 to 1.5 V versus RHE (0.05 V steps −30 s each) and three subsequent cyclic voltammograms were monitored by DEMS. Figure 7a,c show that CO_2 is released at electrode potentials E > 1.20 V versus RHE for the three Pt/C electrocatalysts. However, the released quantity depends strongly on the degree of graphitization of the carbon support: it is maximal for Pt/HSAC and approximately two and four times less for Pt/Vulcan and Pt/RG, respectively. This can be rationalized in view of the preferential electrochemical corrosion of the disordered domains present between the quasi-graphitic carbon crystallites, the weight proportion of which varies as Pt/HSAC ≫ Pt/Vulcan > Pt/RG. It is also noteworthy that the formation of CO_{surf} groups passivates the formation of CO_2 at each electrode potential (note the decreasing oxidation currents over time). In this experiment, three CVs were performed after the staircase potential ramp to mimic the situation which occurs when a PEMFC is restarted. Two CO_2 production peaks were noticed in the positive-going potential sweep. As first shown by Willsau and Heitbaum,[72] and then confirmed by other research groups,[29,31−33] the peak at E ∼ 0.65 V versus RHE should be ascribed to the electrooxidation of CO molecules adsorbed on Pt or to the electrooxidation of CO_{surf} groups located at proximity of the Pt nanoparticles. This peak was also observed on the negative-going potential sweep, albeit of less magnitude. A second peak at E = 1.45 V versus RHE was assigned to the uncatalyzed corrosion of the carbon support.[29,32,72] It is clear from Figure 7b that the Pt-catalyzed carbon corrosion is maximal on Pt/HSAC, less pronounced on Pt/Vulcan, and of meaningless importance on Pt/RG. This result nicely illustrates the dilemma of PEMFC electrocatalysts: poorly structured carbon supports possess high BET surface area therefore allowing homogeneous dispersion of the Pt nanocrystallites, high ECSA values but poor resistance to electrochemical corrosion at elevated electrode potentials. In contrast, the graphitized carbon supports with low BET surface area feature the worst Pt dispersion but possess the highest resistance to electrochemical corrosion during polarization at high electrode potentials.

Finally, TEM images of the fresh and aged Pt/C electrocatalysts were recorded to illustrate how the carbon supports degrade during the FCCJ protocols and to highlight the consequences in terms of Pt dispersion and distribution. Representative pictures obtained after 5000 potential cycles under the load-cycling and the start-up/shutdown protocols are displayed in Figure 8 and Figure 9, respectively. The associated particle size distributions can be found in Figure S1. After the load-cycling protocol, the mean Pt particle size increased for the three Pt/C electrocatalysts (see Figure S1). This result confirms that the load-cycling protocol does not affect significantly the carbon supports and that the electrochemical Ostwald ripening is predominant in this potential region in agreement with the observations derived from Raman spectroscopy and electrochemical techniques. This conclusion is further strengthened by the fact that the monitored ECSA losses are in the same order of magnitude whatever the nature of the carbon support.

In contrast, after the start-up/shutdown protocol, severe degradation of the carbon supports and significant agglomeration of the Pt/C nanocrystallites could be observed in the Raman spectra and TEM images, respectively. This holds especially true for the less organized carbon supports for which the density of isolated—nonagglomerated—Pt nanoparticles drastically decreased relative to the load-cycling protocol, confirming that their detachment was promoted by the corrosion of the carbon support.[34] This conclusion is further

DOI: 10.1021/cs501973j
ACS Catal. 2015, 5, 2184−2194

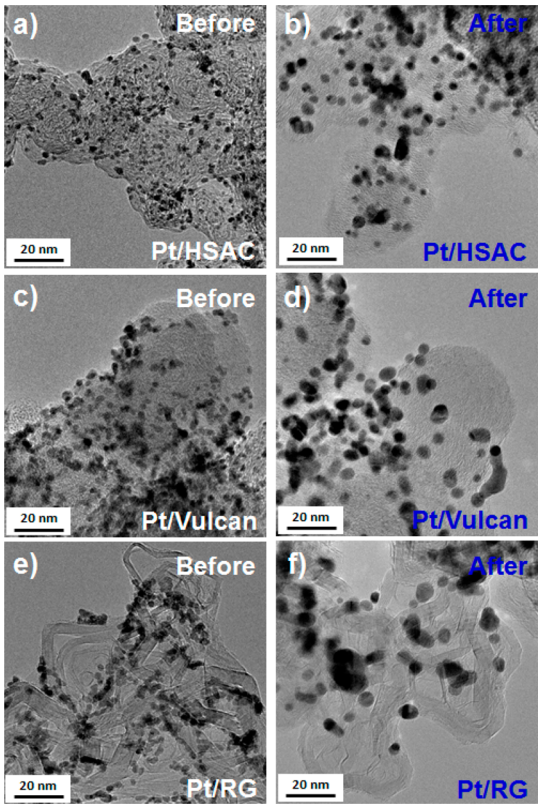

Figure 8. TEM images of the different Pt/C electrocatalysts (a, c, e) before, and (b, d, f) after 5000 "load-cycling" cycles under argon atmosphere.

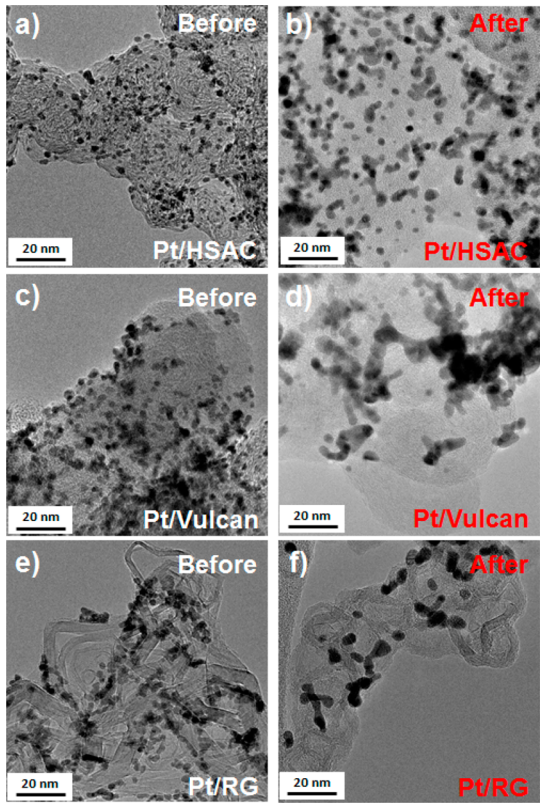

Figure 9. TEM images of the different Pt/C electrocatalysts (a, c, e) before, and (b, d, f) after 5000 "start-up/shutdown" cycles under argon atmosphere.

supported by the emergence of complex Pt nanoparticle shapes and massive Pt agglomerates in the TEM images of the aged Pt/HSAC and Pt/Vulcan electrocatalysts (Figure 9d,e, respectively). The TEM images also illustrate the structural changes, which occurred on the carbon supports. For the HSAC, the classical organization of the carbon blacks (i.e., primary carbon particles – aggregates – agglomerates) was eroded, and the remaining carbon particles appeared amorphous (Figure 9d). Part of this organization was maintained for the Vulcan support, but large areas were found depleted from Pt nanocrystallites after aging. Due to its highly graphitic nature, less morphological changes were noticed on the RG support although some zones evidenced partial amorphization (see Figure 9f).

CONCLUSION

In summary, the degradation of Pt/C electrocatalysts was investigated during AST protocols from the Fuel Cell Commercialization Conference of Japan. The effect of the carbon structure, the potentials limits, and the gas atmosphere were surveyed. The graphitized carbon support (RG) was found to be more resistant to electrochemical corrosion than structurally disordered carbon supports (Vulcan and HSAC). The structure of the carbon support did not impact significantly the ECSA losses during the load-cycling protocol, for which the electrochemical Ostwald ripening was found to be the predominant degradation mechanism. The start-up/shutdown protocol resulted in severe carbon corrosion (preferential oxidation of edge-defects for structurally disordered carbons and formation of edge and surface-defects for the most graphitic ones), as shown by Raman spectroscopy and DEMS. This protocol favored the detachment of the Pt nanoparticles and exacerbated the ECSA losses between the three studied carbon supports. The gas atmosphere negligibly influenced the ECSA losses but affected the surface chemistry of the carbon supports, as shown by combined physical and electrochemical techniques. Although their use implies tremendous work to reoptimize the cathode architecture, graphitized carbon supports appear to be the optimal balance between metal dispersion and limited carbon corrosion for automotive PEMFCs.

ASSOCIATED CONTENT

Supporting Information

The following file is available free of charge on the ACS Publications website at DOI: 10.1021/cs501973j.

The O 1s/C 1s ratio determined by X-ray photoelectron spectroscopy on the fresh Pt/C electrocatalysts and the particle size distributions of the fresh/aged Pt/C electrocatalysts (PDF)

AUTHOR INFORMATION

Corresponding Authors

*E-mail: frederic.maillard@lepmi.grenoble-inp.fr.
*E-mail: laetitia.dubau@lepmi.grenoble-inp.fr.

Notes

The authors declare no competing financial interest.

ACKNOWLEDGMENTS

This work was performed within the framework of the Centre of Excellence of Multifunctional Architectured Materials

DOI: 10.1021/cs501973j
ACS Catal. 2015, 5, 2184–2194

"CEMAM" grant number AN-10-LABX-44-01. The authors acknowledge financial support from the French National Research Agency (grant number ANR-12-PRGE-0007-01), from Oseo-AII (H2E project), FAPESP (Fundacão de Amparo à Pesquisa do Estado de São Paulo − Sao Paulo Research Foundation) − F.H.B.L. − grant numbers 2011/50727-9 and 2013/16930-7, FAPEMA (Fundacão de Amparo à Pesquisa do Estado do Maranhão − Maranhao Research Foundation) grant number BD-01638/13, and CAPES/COFECUB (Project Ph 598/08)

REFERENCES

(1) Nocera, D. G. *ChemSusChem* **2009**, *2*, 387−390.
(2) Katsounaros, I.; Cherevko, S.; Zeradjanin, A. R.; Mayrhofer, K. J. J. *Angew. Chem., Int. Ed.* **2014**, *53*, 102−121.
(3) Mathias, M. F.; Makharia, R.; Gasteiger, H.; Conley, J. J.; Fuller, T. J.; Gittleman, G. J.; Kocha, S. S.; Miller, D. P.; Mittelsteadt, C. K.; Xie, T.; Yan, S. G.; Yu, P. T. *Interface* **2005**, *14*, 24−35.
(4) Guilminot, E.; Corcella, A.; Iojoiu, C.; Berthomé, G.; Maillard, F.; Chatenet, M.; Sanchez, J.-Y. *J. Electrochem. Soc.* **2007**, *154*, B1106−B1114.
(5) Iojoiu, C.; Guilminot, E.; Maillard, F.; Chatenet, M.; Sanchez, J. Y.; Claude, E.; Rossinot, E. *J. Electrochem. Soc.* **2007**, *154*, B1115−B1120.
(6) Ferreira, P. J.; la O', G. J.; Shao-Horn, Y.; Morgan, D.; Makharia, R.; Kocha, S.; Gasteiger, H. A. *J. Electrochem. Soc.* **2005**, *152*, A2256−A2271.
(7) Dubau, L.; Maillard, F.; Chatenet, M.; André, J.; Rossinot, E. *Electrochim. Acta* **2010**, *56*, 776−783.
(8) Dubau, L.; Maillard, F.; Chatenet, M.; Guétaz, L.; André, J.; Rossinot, E. *J. Electrochem. Soc.* **2010**, *157*, B1887−B1895.
(9) Maillard, F.; Dubau, L.; Durst, J.; Chatenet, M.; André, J.; Rossinot, E. *Electrochem. Commun.* **2010**, *12*, 1161−1164.
(10) Dubau, L.; Durst, J.; Maillard, F.; Chatenet, M.; Guétaz, L.; André, J.; Rossinot, E. *Electrochim. Acta* **2011**, *56*, 10658−10667.
(11) Dubau, L.; Durst, J.; Maillard, F.; Chatenet, M.; André, J.; Rossinot, E. *Fuel Cells* **2012**, *12*, 188−198.
(12) Dubau, L.; Guetaz, L.; Durst, J.; Maillard, F.; Chatenet, M.; Andre, J.; Rossinot, E. *ECS Electrochem. Lett.* **2012**, *1*, F13−F15.
(13) Durst, J.; Lamibrac, A.; Charlot, F.; Dillet, J.; Castanheira, L. F.; Maranzana, G.; Dubau, L.; Maillard, F.; Chatenet, M.; Lottin, O. *Appl. Catal., B* **2013**, *138*−*139*, 416−426.
(14) Dubau, L.; Castanheira, L.; Berthomé, G.; Maillard, F. *Electrochim. Acta* **2013**, *110*, 273−281.
(15) Dubau, L.; Lopez-Haro, M.; Castanheira, L.; Durst, J.; Chatenet, M.; Bayle-Guillemaud, P.; Guétaz, L.; Caqué, N.; Rossinot, E.; Maillard, F. *Appl. Catal., B* **2013**, *142*−*143*, 801−808.
(16) Dubau, L.; Castanheira, L.; Maillard, F.; Chatenet, M.; Lottin, O.; Maranzana, G.; Dillet, J.; Lamibrac, A.; Perrin, J.-C.; Moukheiber, E.; ElKaddouri, A.; De Moor, G.; Bas, C.; Flandin, L.; Caqué, N. *Wiley Interdiscip. Rev.: Energy Environ.* **2014**, *3*, 540−560.
(17) Dubau, L.; Castanheira, L.; Chatenet, M.; Maillard, F.; Dillet, J.; Maranzana, G.; Abbou, S.; Lottin, O.; De Moor, G.; El Kaddouri, A.; Bas, C.; Flandin, L.; Rossinot, E.; Caqué, N. *Int. J. Hydrogen Energy* **2014**, *39*, 21902−21914.
(18) Ohma, A.; Shinohara, K.; Iiyama, A.; Yoshida, T.; Daimaru, A. *ECS Trans.* **2011**, *41*, 775−784.
(19) United States Council for Automotive Research, LLC. www.uscar.org/guest/view_team.php?teams_id=17 (accessed July 17th, 2013).
(20) Zana, A.; Speder, J.; Reeler, N. E. A.; Vosch, T.; Arenz, M. *Electrochim. Acta* **2013**, *114*, 455−461.
(21) Zana, A.; Speder, J.; Roefzaad, M.; Altmann, L.; Bäumer, M.; Arenz, M. *J. Electrochem. Soc.* **2013**, *160*, F608−F615.
(22) Schlögl, K.; Hanzlik, M.; Arenz, M. *J. Electrochem. Soc.* **2012**, *159*, B677−B682.
(23) Borup, R.; Meyers, J.; Pivovar, B.; Kim, Y. S.; Mukundan, R.; Garland, N.; Myers, D.; Wilson, M.; Garzon, F.; Wood, D.; Zelenay, P.; More, K.; Stroh, K.; Zawodzinski, T.; Boncella, J.; McGrath, J. E.; Inaba, M.; Miyatake, K.; Hori, M.; Ota, K.; Ogumi, Z.; Miyata, S.; Nishikata, A.; Siroma, Z.; Uchimoto, Y.; Yasuda, K.; Kimijima, K. I.; Iwashita, N. *Chem. Rev.* **2007**, *107*, 3904−3951.
(24) Shao-Horn, Y.; Sheng, W.; Chen, S.; Ferreira, P.; Holby, E.; Morgan, D. *Topics Catal.* **2007**, *46*, 285−305.
(25) Yoda, T.; Uchida, H.; Watanabe, M. *Electrochim. Acta* **2007**, *52*, 5997−6005.
(26) Mayrhofer, K. J. J.; Meier, J. C.; Ashton, S. J.; Wiberg, G. K. H.; Kraus, F.; Hanzlik, M.; Arenz, M. *Electrochem. Com.* **2008**, *10*, 1144−1147.
(27) Meier, J. C.; Katsounaros, I.; Galeano, C.; Bongard, H. J.; Topalov, A. A.; Kostka, A.; Karschin, A.; Schuth, F.; Mayrhofer, K. J. J. *Energy Environ. Sci.* **2012**, *5*, 9319−9330.
(28) Zhao, Z.; Dubau, L.; Maillard, F. *J. Power Sources* **2012**, *217*, 449−458.
(29) Maass, S.; Finsterwalder, F.; Frank, G.; Hartmann, R.; Merten, C. *J. Power Sources* **2008**, *176*, 444−451.
(30) Liu, Z. Y.; Zhang, J. L.; Yu, P. T.; Zhang, J. X.; Makharia, R.; More, K. L.; Stach, E. A. *J. Electrochem. Soc.* **2010**, *157*, B906−B913.
(31) Maillard, F.; Bonnefont, A.; Micoud, F. *Electrochem. Com.* **2011**, *13*, 1109−1111.
(32) Linse, N.; Gubler, L.; Scherer, G. G.; Wokaun, A. *Electrochim. Acta* **2011**, *56*, 7541−7549.
(33) Roen, L. M.; Paik, C. H.; Jarvi, T. D. *Electrochem. Solid-State Lett.* **2004**, *7*, A19−A22.
(34) Park, Y.-C.; Kakinuma, K.; Uchida, M.; Tryk, D. A.; Kamino, T.; Uchida, H.; Watanabe, M. *Electrochim. Acta* **2013**, *91*, 195−207.
(35) Castanheira, L.; Dubau, L.; Mermoux, M.; Berthomé, G.; Caqué, N.; Rossinot, E.; Chatenet, M.; Maillard, F. *ACS Catal.* **2014**, *4*, 2258−2267.
(36) Taniguchi, A.; Akita, T.; Yasuda, K.; Miyazaki, Y. *J. Power Sources* **2004**, *130*, 42−49.
(37) Reiser, C. A.; Bregoli, L.; Patterson, T. W.; Yi, J. S.; Yang, J. D.; Perry, M. L.; Jarvi, T. D. *Electrochem. Solid-State Lett.* **2005**, *8*, A273−A276.
(38) Dillet, J.; Spernjak, D.; Lamibrac, A.; Maranzana, G.; Mukundan, R.; Fairweather, J.; Didierjean, S.; Borup, R. L.; Lottin, O. *J. Power Sources* **2014**, *250*, 68−79.
(39) Kinoshita, K. *Carbon: Electrochemical and physicochemical properties*; John Wiley & Sons: New York, 1988; p 533.
(40) Antonucci, P. L.; Pino, L.; Giordano, N.; Pinna, G. *Mater. Chem. Phys.* **1989**, *21*, 495−506.
(41) Stonehart, P. *Carbon* **1984**, *22*, 423−431.
(42) Cherstiouk, O. V.; Simonov, A. N.; Moseva, N. S.; Cherepanova, S. V.; Simonov, P. A.; Zaikovskii, V. I.; Savinova, E. R. *Electrochim. Acta* **2010**, *55*, 8453−8460.
(43) Artyushkova, K.; Pylypenko, S.; Dowlapalli, M.; Atanassov, P. *J. Power Sources* **2012**, *214*, 303−313.
(44) Knight, D. S.; White, W. B. *J. Mater. Res.* **1989**, *4*, 385−393.
(45) Takahashi, I.; Kocha, S. S. *J. Power Sources* **2010**, *195*, 6312−6322.
(46) Teliska, M.; Murthi, V. S.; Mukerjee, S.; Ramaker, D. E. *J. Phys. Chem. C* **2007**, *111*, 9267−9274.
(47) Herrmann, C. C.; Perrault, G. G.; Pilla, A. A. *Anal. Chem.* **1968**, *40*, 1173−1174.
(48) Castanheira, L.; Dubau, L.; Maillard, F. *Electrocatalysis* **2013**, 1−11.
(49) Tuinstra, F.; Koenig, J. L. *J. Chem. Phys.* **1970**, *53*, 1126−1130.
(50) Gruber, T.; Zerda, T. W.; Gerspacher, M. *Carbon* **1994**, *32*, 1377−1382.
(51) Hara, M.; Lee, M.; Liu, C.-H.; Chen, B.-H.; Yamashita, Y.; Uchida, M.; Uchida, H.; Watanabe, M. *Electrochim. Acta* **2012**, *70*, 171−181.
(52) Bett, J. A.; Kinoshita, K.; Stonehart, P. *J. Catal.* **1974**, *35*, 307−316.
(53) Heckman, F. A. *Rubber Chem. Technol.* **1969**, *37*, 1245.
(54) Heidenreich, R. D.; Hess, W. M.; Ban, L. L. *J. Appl. Crystallogr.* **1968**, *1*, 1.

DOI: 10.1021/cs501973j
ACS Catal. 2015, 5, 2184−2194

(55) Miyazaki, K.; Shirakata, H.; Abe, T.; Yoshizawa, N.; Ogumi, Z. *Fuel Cells* **2010**, *10*, 960−965.
(56) Job, N.; Maillard, F.; Marie, J.; Berthon-Fabry, S.; Pirard, J. P.; Chatenet, M. *J. Mater. Sci.* **2009**, *44*, 6591−6600.
(57) Job, N.; Lambert, S.; Chatenet, M.; Gommes, C. J.; Maillard, F.; Berthon-Fabry, S.; Regalbuto, J. R.; Pirard, J. P. *Catal. Today* **2010**, *150*, 119−127.
(58) Job, N.; Chatenet, M.; Berthon-Fabry, S.; Hermans, S.; Maillard, F. *J. Power Sources* **2013**, *240*, 294−305.
(59) Cao, C.; Yang, G.; Dubau, L.; Maillard, F.; Lambert, S. D.; Pirard, J. P.; Job, N. *Appl. Catal., B* **2014**, *150−151*, 101−106.
(60) Rooke, J.; De Matos Passos, C.; Chatenet, M.; Sescousse, R.; Budtova, T.; Berthon-Fabry, S.; Mosdale, R.; Maillard, F. *J. Electrochem. Soc.* **2011**, *158*, B779−B789.
(61) Patterson, T. W.; Darling, R. M. *Electrochem. Solid-State Lett.* **2006**, *9*, A183−A185.
(62) Carter, R. N.; Gu, W.; Brady, B.; Yu, P. T.; Subramanian, K.; Gasteiger, H. A. In *Handbook of Fuel Cells - Fundamentals, Technology and Applications*; Vielstich, W., Lamn, A., Gasteiger, H. A., Eds.; John Wiley & Sons: New York, 2009; Vol. *6*, pp 829−843.
(63) Ishigami, Y.; Takada, K.; Yano, H.; Inukai, J.; Uchida, M.; Nagumo, Y.; Hyakutake, T.; Nishide, H.; Watanabe, M. *J. Power Sources* **2011**, *196*, 3003−3008.
(64) Maillard, F.; Simonov, P.; Savinova, E. R. In *Carbon Materials for Catalysis*; Serp, P., Figueiredo, J. L., Eds.; John Wiley & Sons, Inc.: New York, 2009; Vol. *5*, pp 429−480.
(65) Nikkuni, F. R.; Vion-Dury, B.; Dubau, L.; Maillard, F.; Ticianelli, E. A.; Chatenet, M. *Appl. Catal., B* **2014**, *156−157*, 301−306.
(66) Oh, H.-S.; Lim, K. H.; Roh, B.; Hwang, I.; Kim, H. *Electrochim. Acta* **2009**, *54*, 6515−6521.
(67) Vinod Selvaganesh, S.; Selvarani, G.; Sridhar, P.; Pitchumani, S.; Shukla, A. K. *Fuel Cells* **2011**, *11*, 372−384.
(68) Zhao, X.; Hayashi, A.; Noda, Z.; Kimijima, K. i.; Yagi, I.; Sasaki, K. *Electrochim. Acta* **2013**, *97*, 33−41.
(69) Zhao, Z.; Castanheira, L.; Dubau, L.; Berthomé, G.; Crisci, A.; Maillard, F. *J. Power Sources* **2013**, *230*, 236−243.
(70) Sze, S. K.; Siddique, N.; Sloan, J. J.; Escribano, R. *Atmos. Environ.* **2001**, *35*, 561−568.
(71) Hiramitsu, Y.; Sato, H.; Hosomi, H.; Aoki, Y.; Harada, T.; Sakiyama, Y.; Nakagawa, Y.; Kobayashi, K.; Hori, M. *J. Power Sources* **2010**, *195*, 435−444.
(72) Willsau, J.; Heitbaum, J. *J. Electroanal. Chem. Interfacial Electrochem.* **1984**, *161*, 93−101.

DOI: 10.1021/cs501973j
ACS Catal. 2015, 5, 2184−2194